hydrology

MDPI

Article

Climate Change Projections of Potential Evapotranspiration for the North American Monsoon Region

Eylon Shamir [1,*], Lourdes Mendoza Fierro [2], Sahar Mohsenzadeh Karimi [2], Norman Pelak [1], Emilie Tarouilly [1], Hsin-I Chang [2] and Christopher L. Castro [2]

[1] Hydrologic Research Center, San Diego, CA 92127, USA; npelak@hrcwater.org (N.P.); etarouilly@hrcwater.org (E.T.)
[2] Department of Hydrology and Atmospheric Sciences, University of Arizona, Tucson, AZ 85721, USA; mkarimi@arizona.edu (S.M.K.); hchang05@arizona.edu (H.-I.C.); clcastro@arizona.edu (C.L.C.)
* Correspondence: eshamir@hrcwater.org

Abstract: We assessed and quantified future projected changes in terrestrial evaporative demand by calculating Potential Evapotranspiration (PET) for the North American Monsoon region in the Southwestern U.S. and Mexico. The PET projections were calculated using the daily Penman–Monteith equation. The terrestrial meteorological variables needed for the equation (i.e., minimum and maximum daily temperature, specific humidity, wind speed, incoming shortwave radiation, and pressure) were obtained from the North American–CORDEX initiative. We used dynamically downscaled projections of three CMIP5 GCMs for RCP8.5 emission scenarios (i.e., HadGEM2-ES, MPI-ESM-LR, and GFDL-ESM2M), and each was dynamically downscaled to ~25 km by two RCMs (i.e., WRF and regCM4). All terrestrial annual PET projections showed a statistically significant increase when comparing the historical period (1986–2005) to future projections (2020–2039 and 2040–2059). The regional spatial average of the six GCM-RCM combinations projected an increase in the annual PET of about +4% and +8% for 2020–2039 and 2040–2059, respectively. The projected average 20-year annual changes over the study area range for the two projection periods were +1.4%–+8.7% and +3%–+14.2%, respectively. The projected annual PET increase trends are consistent across the entire region and for the six GCM-RCM combinations. Higher annual changes are projected in the northeast part of the region, while smaller changes are projected along the pacific coast. The main drivers for the increase are the projected warming and increase in the vapor pressure deficit. The projected changes in PET, which represent the changes in the atmospheric evaporative demand, are substantial and likely to impact vegetation and the hydrometeorological regime in the area. Quantitative assessments of the projected PET changes provided by this study should be considered in upcoming studies to develop resilience plans and adaptation strategies for mitigating the projected future changes.

Keywords: climate change; potential evapotranspiration; North American Monsoon; NA-CORDEX; Penman–Monteith

check for updates

Citation: Shamir, E.; Mendoza Fierro, L.; Mohsenzadeh Karimi, S.; Pelak, N.; Tarouilly, E.; Chang, H.-I.; Castro, C.L. Climate Change Projections of Potential Evapotranspiration for the North American Monsoon Region. *Hydrology* **2024**, *11*, 83. https://doi.org/10.3390/hydrology11060083

Academic Editors: Aristoteles Tegos and Nikolaos Malamos

Received: 18 May 2024
Revised: 9 June 2024
Accepted: 12 June 2024
Published: 14 June 2024

Copyright: © 2024 by the authors. Licensee MDPI, Basel, Switzerland. This article is an open access article distributed under the terms and conditions of the Creative Commons Attribution (CC BY) license (https://creativecommons.org/licenses/by/4.0/).

1. Introduction

Climate change impacts on rainfall and temperature patterns, and the effect of these changes in the North American Monsoon (NAM) region (Southwestern U.S. and Mexico) is an active research topic [1–6]. While the effects on precipitation are well studied, a less studied topic, which is the focus of this study, is the impact of climate change on the atmospheric evaporative demand (AED) in the NAM region. The AED represents the upper limit of actual evapotranspiration when water availability is unlimited. Changes in AED impact the hydrological cycle to alter water resource availability, soil moisture conditions, runoff production from rainfall events, water storage in surface and subsurface reservoirs, vegetative land cover, and drought severity. AED is linked to the NAM dynamics by influencing the interplay between enhancing tropospheric stability, which suppresses

convection to increase evaporation, which, in turn, increases moisture for convective activity [3]. Moreover, evapotranspiration in the NAM region is a major source of moisture for convective precipitation events [7,8].

Projecting changes in future AED is a challenging task because it depends on changes in various near-surface atmospheric variables that represent the radiative and aerodynamic state of the atmosphere. The radiative state represents the energy available to vaporize water, and it is estimated by temperature and net radiation. The aerodynamic state represents the capacity of the air to store and remove water and is estimated by wind and vapor pressure deficit. A common method used to assess the AED involves estimating the Potential Evapotranspiration (PET), which is the evaporation that would occur when a sufficient water source is available on the land surface.

A review of 55 worldwide studies of observed pan evaporation datasets pointed to declining evaporation since the second half of the 20th century [9]. This historical declining trend, as measured by pan evaporation, was also shown in several studies from the Southwestern U.S. and Mexico [10–14]. This reduction in evaporative demand may be seen as counterintuitive to the concurrent observed warming trend [6,11,15]. The causes for the decline in pan evaporation remain inconclusive, and various explanations have been provided, such as an increase in cloudiness that, in conjunction with the presence of aerosols, causes a reduction in shortwave radiation [16,17]; changes in aerodynamic components such as reduced wind speeds [14,16,18] and a decreased vapor pressure deficit [19]; and impacts on other factors, such as declines in El Nino Southern Oscillation and cyclical sunspot activity [11,13].

Another possible reason for the observed historical decline may be attributed to the deficiencies of pan evaporation for representing AED in water-limited environments. This is because in these water-limited regions, the unused energy at the land surface increases the sensible heat flux from the ground, a process that is not accounted for in pan evaporation [20].

Notwithstanding the observed historical declining trend, using output from global climate models (GCMs), Cook et al. [21] projected globally widespread increases in PET. The projected future PET increase was attributed to projected increases in surface net radiation and vapor pressure deficit. The highest PET increases are projected for the mid-latitudes of the Northern Hemisphere and in western North America, Europe, and southeast China. Other GCM studies for the conterminous U.S. also projected PET increases [22,23]. In Mexico, Martinez-Sifuentes et al. [24] projected an increase in PET for the northern parts of the state of Durango in north–central Mexico using a PET equation that considers only air surface temperature. Mundo-Molina [25] projected an increase in annual PET that could reach 8% in Northern Mexico for a climate change scenario of a temperature increase of 3 °C over the entire country.

The NAM region is dominated by regional (mesoscale) processes, the representation of which is relatively challenging with coarse GCMs [26–30]. Dynamical downscaling with regional climate models (RCMs) for longer-term climate simulations has shown skill in capturing climate variability, depending on the region of study and storm types [31,32]. For future climate projections, dynamical downscaling with RCMs generally improves the representation of mean precipitation changes and convective precipitation [33,34] compared to GCM projections.

In this study, we assess the projected changes in annual and monthly PET over the NAM region. To project the future PET, we used daily terrestrial meteorological variables from dynamically downscaled simulations of six GCM-RCM combinations as inputs for the daily Penman–Monteith equation. The GCMs are from the Coupled Model Intercomparison Project Phase 5 (CMIP5). They were forced by Representative Concentration Pathways 8.5 (RCP8.5) emission scenarios.

2. Materials and Methods

Historical Dataset. We used the TerraClimate dataset [35] to calculate the climatological PET over the NAM region. TerraClimate is a ~4 km (1/24th degree) monthly climatological dataset of global terrestrial surface meteorological fluxes (i.e., maximum and minimum temperature, vapor pressure, precipitation accumulation, downward surface shortwave radiation, and wind speed), containing data going back to 1958. To our knowledge, this is the only observation-based spatial climatological dataset that includes all the terrestrial variables needed as inputs for the FAO-56 equation.

While we believe the TerraClimate dataset is the most appropriate observational dataset for this type of study, we recognize its sources of epistemic uncertainties. The main sources of uncertainties in the PET estimates are the large differences in the number of observation stations among the various meteorological variables, the variety of sources of data with differences in quality and reporting times, and the uncertainties associated with the selection of the interpolating and extrapolating procedures. In addition, the standardized reference evapotranspiration equation used herein is a nonlinear equation, and therefore, the use of monthly average variables to calculate daily PET would not exactly yield the average monthly PET values calculated daily.

Climate Model Datasets (Historical and Projected). Dynamically downscaled climate projections from the CMIP5 GCMs are available from the North America Coordinated Regional Climate Downscaling Experiment (NA-CORDEX) program [36,37], an initiative sponsored by the World Climate Research Program to provide regional climate downscaling data for regional climate change adaptation and impact assessment. Although the Intergovernmental Panel on Climate Change (IPCC) has already published the Sixth Assessment Report (AR6), published in 2021, as of April 2024, dynamically downscaled projections of the GCM simulations that supported the IPCC Sixth Assessment Report (AR6) are not available for the study region.

Projections from three NA-CORDEX GCMs, forced by the Representative Concentration Pathway (RCP) 8.5 greenhouse gas and aerosol emission scenario, were dynamically downscaled. The GCMs used were the HadGEM2-ES (Global Environmental Model, version 2, from the United Kingdom Meteorological Office, Hadley Centre); the MPI-ESM-LR (Earth System Model), running on the low-resolution (LR) grid from the Max Planck Institute for Meteorology; and the GFDL-ESM2M from the NOAA Geophysical Fluid Dynamics Laboratory, using the Earth System Model version 2.

These three GCMs were selected because of their representation of a range of North American climate sensitivities [38,39]. They were also found to represent the global air temperature, atmospheric pressure, wind, solar radiation patterns, the Western U.S. regional temperature, precipitation, sea level pressure, and El Niño/Southern Oscillation variability well [40]. Moreover, the selected GCMs were found to represent the large-scale synoptic features of the NAM [30]. These GCMs were previously used in numerous climate impact assessments for the region [5,41–45].

The GCM outputs were dynamically downscaled to a 25 km horizontal grid resolution using two different regional climate models (RCMs). The first RCM we used was the Advanced Research version of the Weather Research and Forecasting (WRF) model, version 3.4 [46], which is supported by the National Center for Atmospheric Research. The configuration, parameterization, and validation of the WRF model is described in [27,33]. The second RCM we used, RegCM4, is supported by the Regional Climate Research Network, a network of scientists coordinated by the Earth System Physics section of the Abdus Salam International Centre for Theoretical Physics (ICTP http://users.ictp.it/RegCNET/, accessed on 18 May 2024). The projections cover two future horizon periods (i.e., 2020–2039 and 2040–2059), which were compared to the simulated historical period of 1986–2005. The CMIP5 GCMs simulated the historical period for 1950–2005 and the future projections for 2006–2100.

PET Equation. To estimate PET, we used the FAO-56 reference crop PET equation that is often named the standardized reference evapotranspiration equation [47]. Contrary to ET,

which represents an upward water flux from soil, free water, and vegetation, PET indicates the demand of water from the atmosphere and is calculated using terrestrial meteorological variables that represent both the radiative and aerodynamic state of the atmosphere. The FAO-56 reference crop equation was developed to estimate evapotranspiration from a well-watered vegetated surface using the Penman–Monteith equation for a reference crop with a height of 0.12 m, surface resistance of 70 s m^{-1}, and albedo of 0.23. The FAO-56 PET equation accounts for both radiative and aerodynamic near-surface atmospheric components.

The FAO-56 equation for daily PET in millimeters is written as follows:

$$PET = \frac{0.408\Delta(R_n - G) + \gamma \frac{900}{T_a+273} u_2 VPD}{\Delta + \gamma(1 + 0.34u_2)} \quad (1)$$

where R_N is net daily radiation at the vegetated surface (MJ m^{-2} d^{-1}), calculated as the difference between incoming net shortwave radiation and outgoing net longwave radiation (as described in [47]); G is the heat flux in the ground (MJ m^{-2} d^{-1}), which is assumed to be negligible at the daily time scale; Δ is the slope of the vapor pressure as a function of the temperature curve (kPa $°C^{-1}$); γ is the psychrometric constant (kPa $°C^{-1}$); Ta is the mean daily air temperature (°C); VPD is the vapor pressure deficit (kPa), which is calculated as the difference between the saturated and actual vapor pressure; and u_2 is the average daily wind speed at 2 m aboveground elevation (m s^{-1}). The daily near-surface (i.e., 2 m elevation aboveground) atmospheric variables required as inputs for the equation are temperature, incoming shortwave radiation, specific humidity, wind speed, and atmospheric pressure. The implementation of this equation followed the procedure outlined by Allen et al. [47].

PET Projections. Quantitative historical PET simulations by climate models are often inaccurate because of biases in the simulated meteorological variables, and consequently, the PET quantitative projections of the future period are highly uncertain [48,49]. Thus, in this analysis, rather than looking at quantitative PET projections, we assessed the percent changes from the historical to the future periods of interest. The relative changes were calculated as the ratio between the difference of the future and historical periods and the historical period, as expressed in the equation below:

$$\delta PET(dur) = \frac{PET(dur)_{future} - PET(dur)_{historical}}{PET(dur)_{historical}} \times 100 \quad (2)$$

where δ is the calculated change in percent (%), dur indicates the duration of the analysis of change (e.g., monthly, seasonal, annual), and the future and historical subscripts refer to the periods of the climate model simulations.

3. Results

3.1. Observed PET

Figure 1 shows the annual PET climatology that was calculated using the FAO-56 equation (Equation (1)) for the period of 1986–2005. During the 20-year period of record, the regional average annual PET values range from 750 to 2436 mm/year, with a regional average of 1456 mm/year. The highest annual PET values are found in southeastern California and western Arizona, and there is another high-evaporation region that is centered at the southeast border of New Mexico, with a clear decline in the northward and eastward directions. Regarding our evaluation of the PET intra-annual variability, in Figure 2, the spatial distribution of the PET maximum, that of the PET minimum, and their difference are shown. The regional average of the annual range of PET difference is 266 mm/year, with the lowest and highest differences being 69 and 397 mm/year, respectively. For most of Mexico, the PET difference between the maximum and the minimum annual PET does not exceed 200 mm/year, while wider ranges are found north of the U.S.–Mexico border, with the highest differences in Kansas and northern Nevada. While these differences in the PET ranges between the two countries may be attributed to

the different climates, they may also be attributed to the differences in the datasets that are available from the two countries that contributed to the TerraClimate product. Figure 3 shows the 20-year average climatology for the meteorological variables (precipitation, temperature, incoming solar radiation, wind speed, and vapor pressure deficit) used in the FAO-56 equation (Equation (1)).

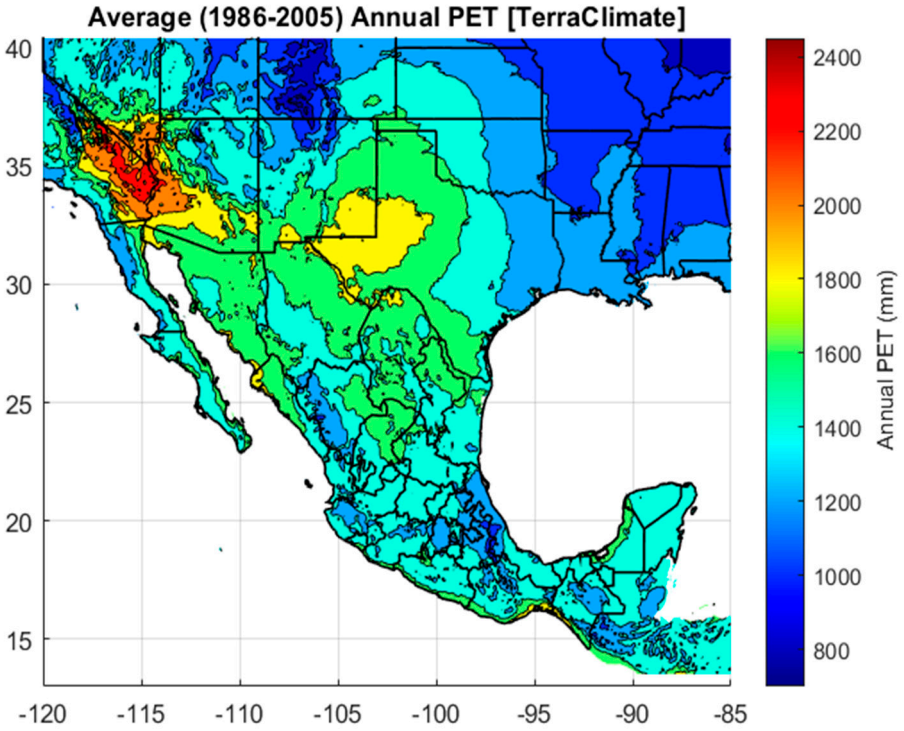

Figure 1. Annual 1986–2005 average PET calculated from the monthly data of the TerraClimate dataset.

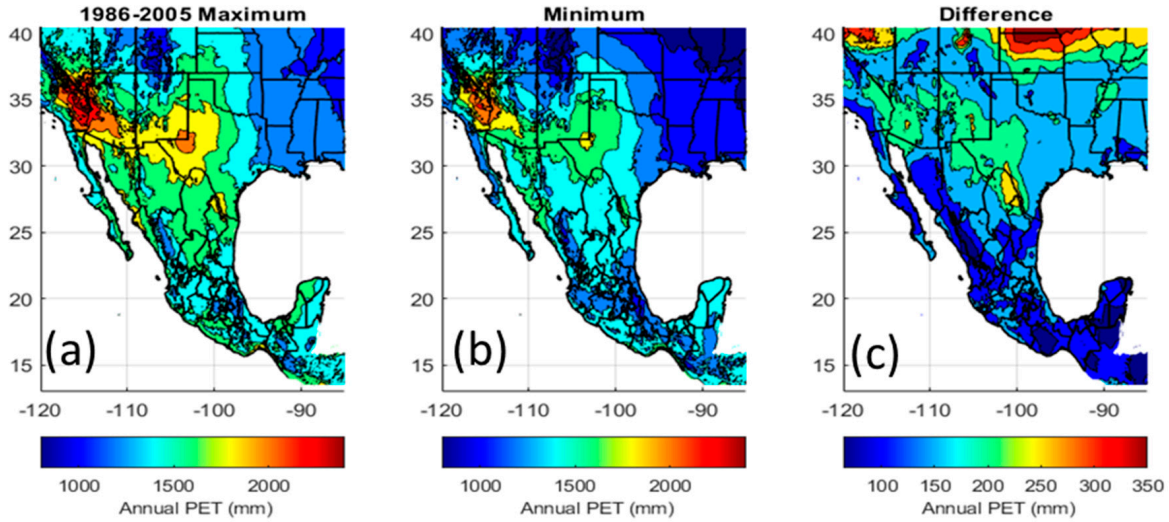

Figure 2. Maximum (**a**), minimum (**b**), and difference between maximum and minimum (**c**) of 1986–2005 average annual PET from TerraClimate.

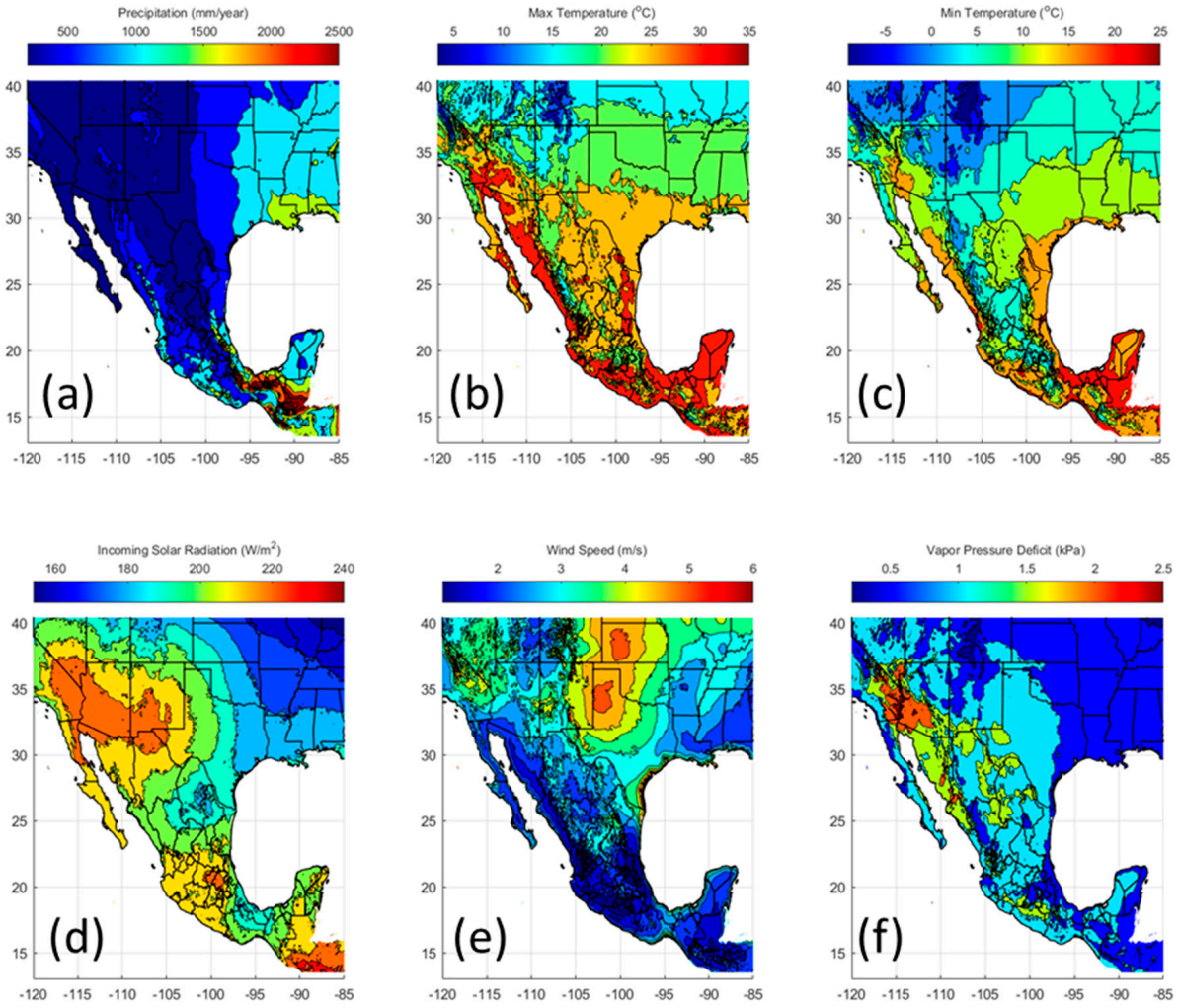

Figure 3. Annual averages (1986–2005) for precipitation (**a**), maximum (**b**) and minimum (**c**) daily temperature, daily incoming solar radiation (**d**), wind speed (**e**), and vapor pressure deficit (**f**) from TerraClimate.

3.2. PET Projections

Figure 4 (upper panels) shows the 20-year arithmetic average of the annual PET changes between the historical period and each of the two future projection periods (2020–2039 and 2040–2059, respectively). The average annual changes and other statistical indices were calculated for each grid cell, for each of the six GCM-RCM projections, and for each of the 400 combinations (20 historical years × 20 projection years), i.e., from a statistical sample that contains a total of 2400 estimates of percent annual changes. Figure 4 shows that PET is projected to increase across the entire North American Monsoon region. This PET increase is more pronounced during the second projection period (2040–2059). The regions that are projected to have the highest changes are the high-elevation mountain ranges along the Sierra Madre Occidental, Sierra Madre del Sur, and Sierra Madre Oriental, while smaller changes are projected in the Central Mexican Plateau and along the Pacific coast.

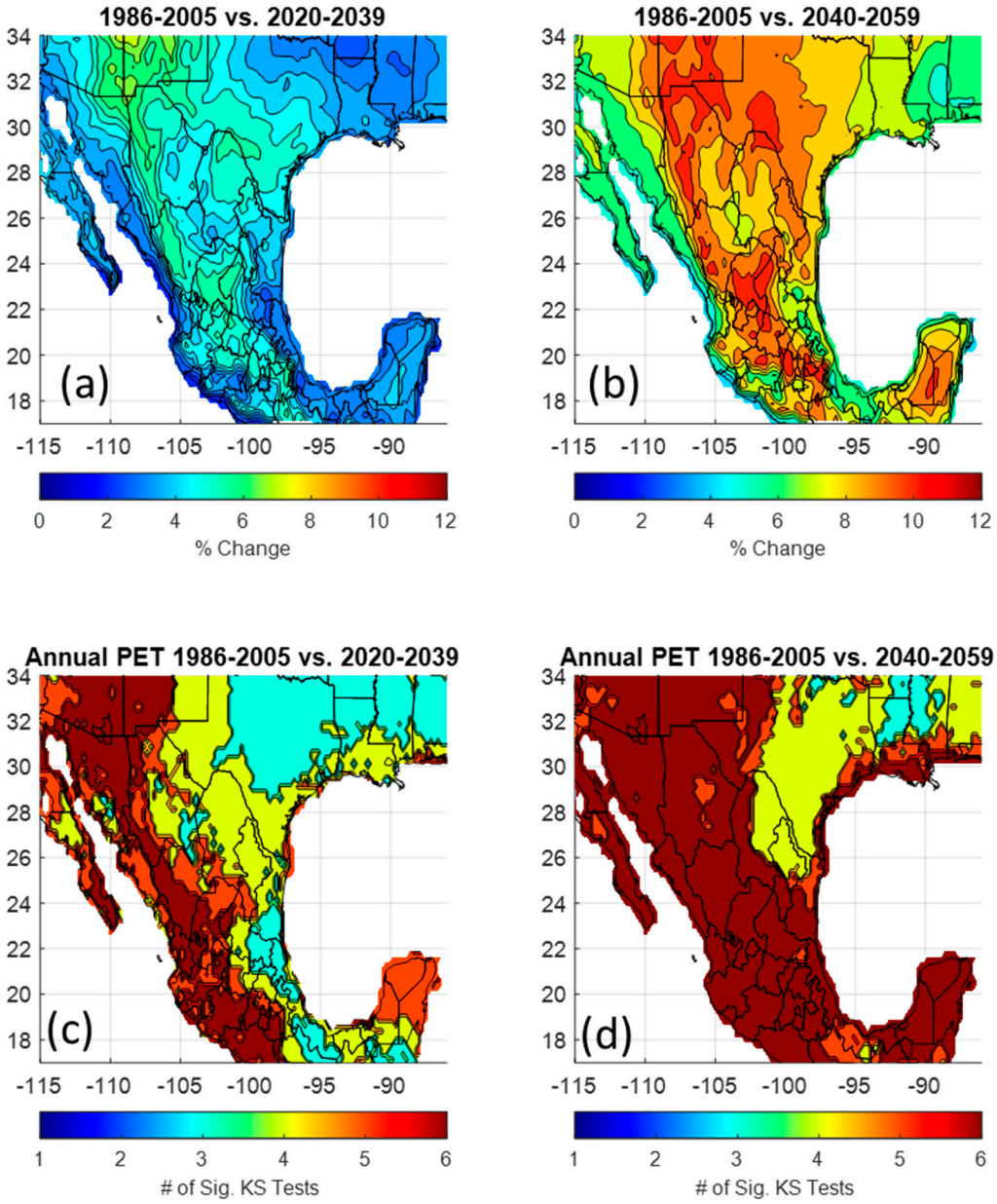

Figure 4. Projected annual changes in PET for the NAM region from 1986–2005 to 2020–2039 (**a**) and 1986–2005 to 2040–2059 (**b**). The upper plots are the 20-year average annual percent changes projected by the six NA-CORDEX climate models. The lower plots (**c**,**d**) are the number of models (out of six) that yielded a significant difference in the annual PET between the historical period and the future projections using a KS test (alpha = 0.05).

In the lower panels of Figure 4, the number of models (out of the six GCM-RCM projections used in this study) that projected future changes significantly different from the simulated historical period (1985–2005) are shown. Statistical significance was calculated based on a two-sample non-parametric Kolmogorov–Smirnov (KS) hypothesis test, with $\alpha = 0.05$. The KS significance test results were comparable to results obtained from Student's *t*-test). We found that at least three of the six projections showed that the projected PET was significantly different from the distribution of the simulated historical period. For the second future period (2040–2059), the annual PET projections in most of the region were found to be significantly different from the historical period by all six projections.

The area with the strongest agreement among the models on the projected future being significantly different than the historical period is the longitudinal band that includes the

Sierra Madre Occidental and Sierra Madre Del Sur. In general, the 2020–2039 projections of annual PET changes have an overall west-to-east pattern. In the western coastal region, the annual PET changes are projected to be less than 5%, while farther east, towards the Sierra Madre Occidental, the projected changes are about 7–8%. The projected changes decrease eastward towards the Mexican Plateau and increase again at the Sierra Madre Oriental. A similar pattern is shown for the 2040–2059 projections but with larger projected annual changes that exceed 15%.

Table 1 summarizes the annual PET regional statistics of the six climate models. It can be seen that the average projected changes for 2020–2039 and 2040–2059 over the study area are 4.0% and 7.0%, respectively. It is interesting to note that although the signal shows a projected increase in annual PET overall, averages of only 77% and 87% for the statistical samples show positive changes for 2020–2039 and 2040–2059, respectively.

Table 1. Areal averages of PET change statistics.

	2020–2039	**2040–2059**
Average	4.0%	7.0%
Median	3.6%	6.5%
95th percentile	14.9%	18.5%
Minimum 20-year average	1.4%	3.0%
Maximum 20-year average	8.7%	14.2%
5th percentile	−5.4%	−2.6%
Standard deviation	6.2%	6.5%
Positive change	77%	87%

To represent the spatial variability of the spread in the distribution of projected annual PET changes, Figure 5 shows the ranges between the 95th and 5th percentiles of the annual PET changes for the two projection periods. Although there is a clear increase in the annual PET changes from the near future to the far future, the spatial distribution of the annual PET changes is similar between the two projection periods. An interesting pattern seen in this plot is the generally increasing gradient from west to east and south to north. We note that the largest ranges of annual changes, which are larger than 55%, are seen in the northeast, while smaller ranges (<10%) are seen, for example, along the Pacific coast. These differences in ranges can be attributed to the greater inter-annual variability of the annual PET, as captured in Figure 2. However, these ranges may also be attributed to the uncertainty that stems from the differences among the climate projections, which is explored in the following analysis.

In Figure 6, we show scatter plots of all the climate models' grid cell projected average changes in annual PET as a function of the (a) grid cells' elevation and (b) the six-model simulated historical average annual PET (mm/year). It is seen that the projected annual PET changes are positively correlated with the grid cell elevation (correlation coefficients, R, of 0.62 and 0.75 for the near and far future, respectively). On the other hand, the projected annual change in PET is negatively correlated with the historical simulations of the annual PET (R values of −0.46 and −0.59 for the near and far future, respectively). These two factors (elevation and historical simulations), despite exhibiting substantial correlations, as seen by the large scatter in Figure 6, are limited predictors of the projected annual change. It can also be observed that the GCMs that were downscaled using RegCM showed considerably higher correlations than those downscaled using WRF.

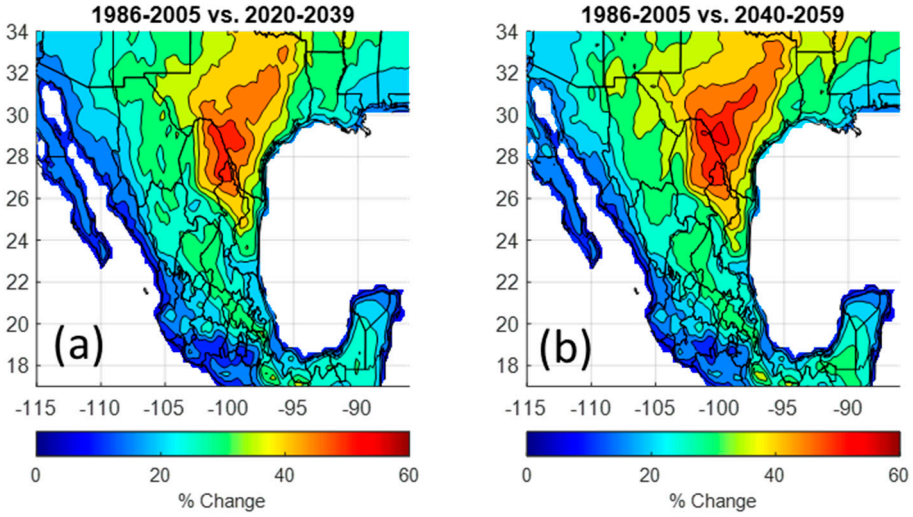

Figure 5. Areal statistics of the projected annual PET expressed as the range of change between the 95th and 5th percentiles as projected for 2020–2039 (**a**) and 2040–2059 (**b**).

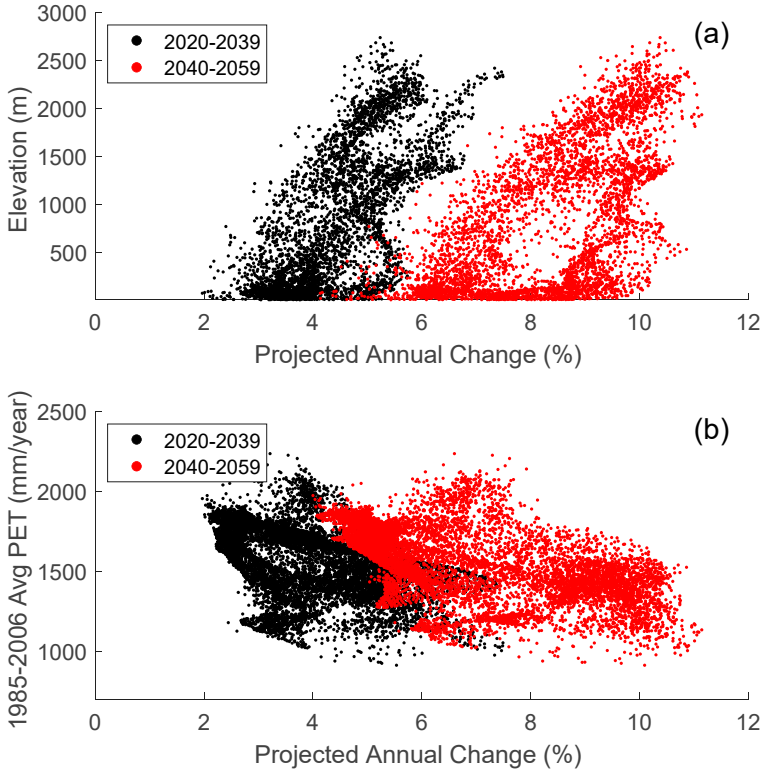

Figure 6. The annual PET changes as a function of elevation (**a**) and average simulated historical annual PET (**b**).

In Figures 7 and 8, we show the projected annual PET changes for each of the six combinations of GCMs and RCMs for 2020–2039 and 2040–2059, respectively. All six model combinations projected overall positive changes in annual PET over most of the region. It can also be seen that within individual models, the annual PET increases from the early to mid-21st century (Figures 7 and 8, respectively). However, the models do not always agree among themselves on the spatial pattern of the annual PET changes. In general, the GCMs that were downscaled with the RegCM model show annual PET changes that tend to be larger than those of the GCMs that were downscaled with WRF. For instance, in southern Texas, while the GFDL-RegCM and MPI-WRF combinations showed the lowest changes, the MPI-RegCM, Had-RegCM, and GFDL-WRF showed the largest projected changes.

Another example of a notable difference is seen between MPI-WRF and GFDL-WRF in the eastern region. This may be caused by differences among models in their representation of the regional atmosphere and surface meteorological variables. In this study, we assumed that the six climate models are equally skillful in their PET simulations. Thus, although all models agree that PET is projected to increase, the spatial distribution of the changes is rather uncertain.

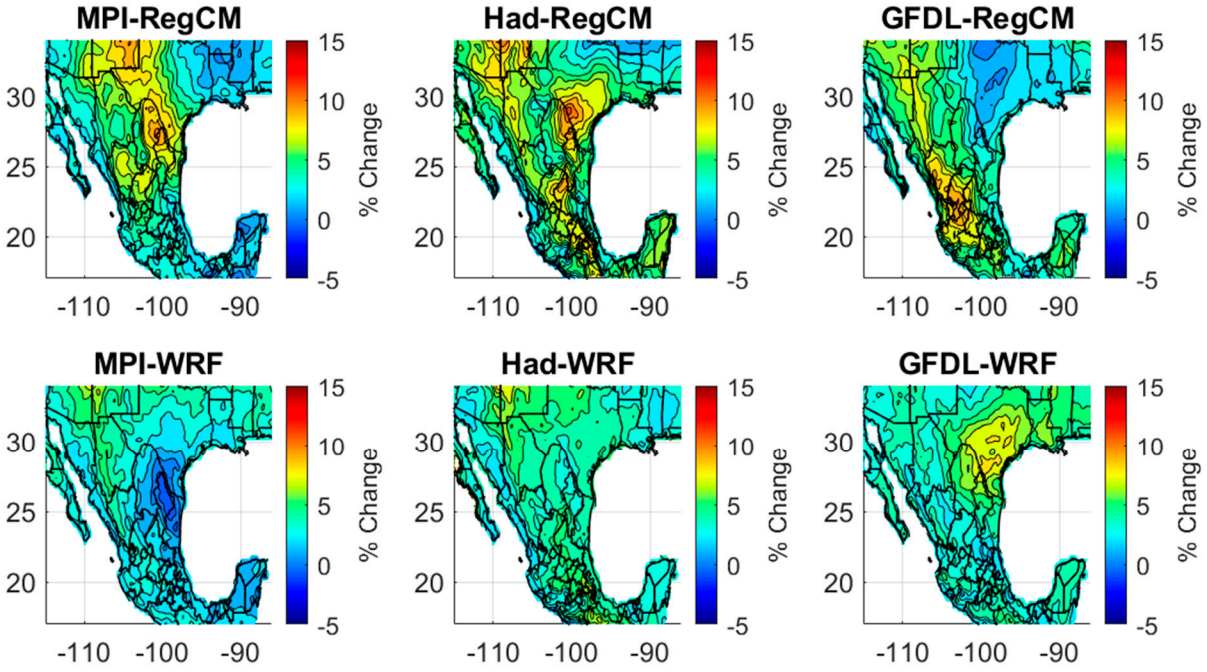

Figure 7. Average projected annual change in PET (%) for the six GCM-RCM combinations for 2020–2039.

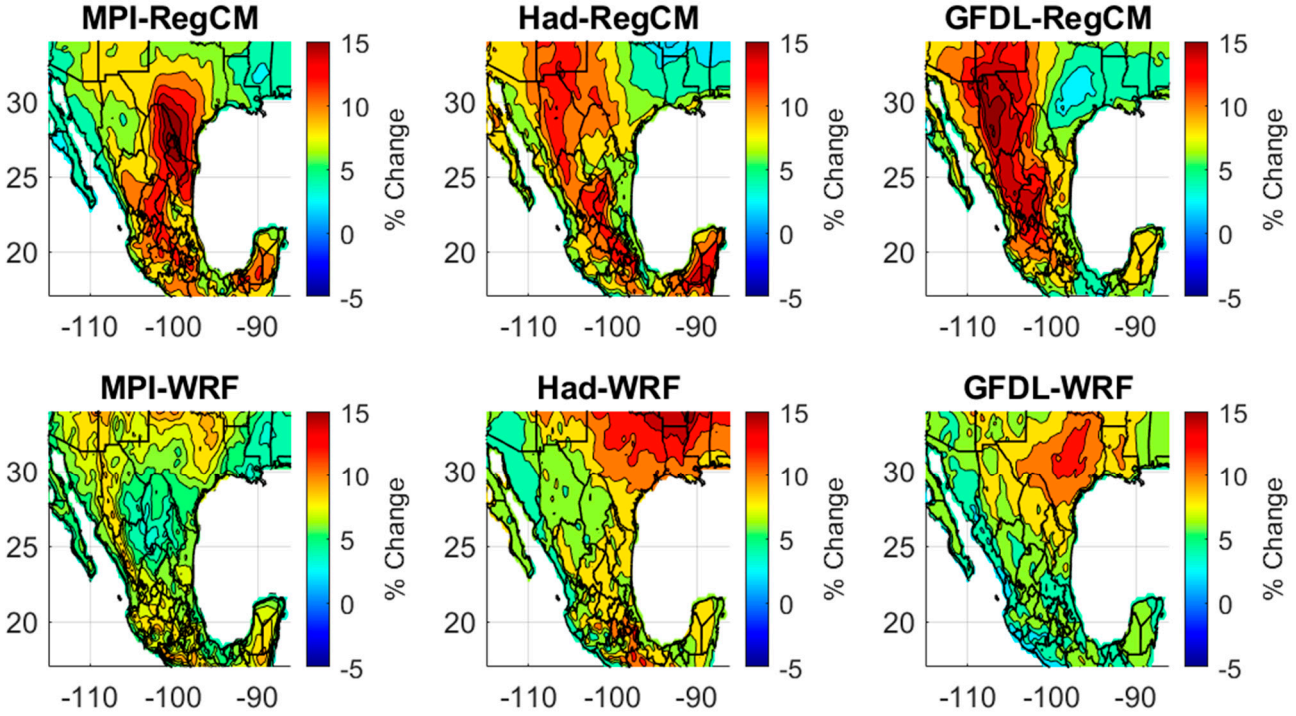

Figure 8. As in Figure 7 but for 2040–2059.

In order to assess the main causes for the projected annual PET increases, we analyzed the changes in the meteorological variables used as inputs for the PET equation (Figure 9). As expected, both minimum and maximum temperature show large projected warming. The projected annual changes in wind speed and surface radiation were not found to be significantly different from those for the historical period. Specific humidity also displays a clear increase, which is associated with temperature because warmer air can hold more water vapor. Increases in specific humidity for a given temperature decrease the vapor pressure deficit (VPD), which, as can be seen in Equation (1), decreases the daily PET. The VPD (i.e., the difference between the actual specific humidity and the specific humidity at saturation) indicates the maximum amount of water that can be evaporated. The sensitivity of VPD to changes in temperature and specific humidity, as calculated with the Clausius–Clapeyron equation, is demonstrated in Figure 10. For a given temperature, an increase in the actual specific humidity, as expected, decreases the VPD. However, increases in temperature for a given specific humidity increase the VPD, which, in turn, increases the PET.

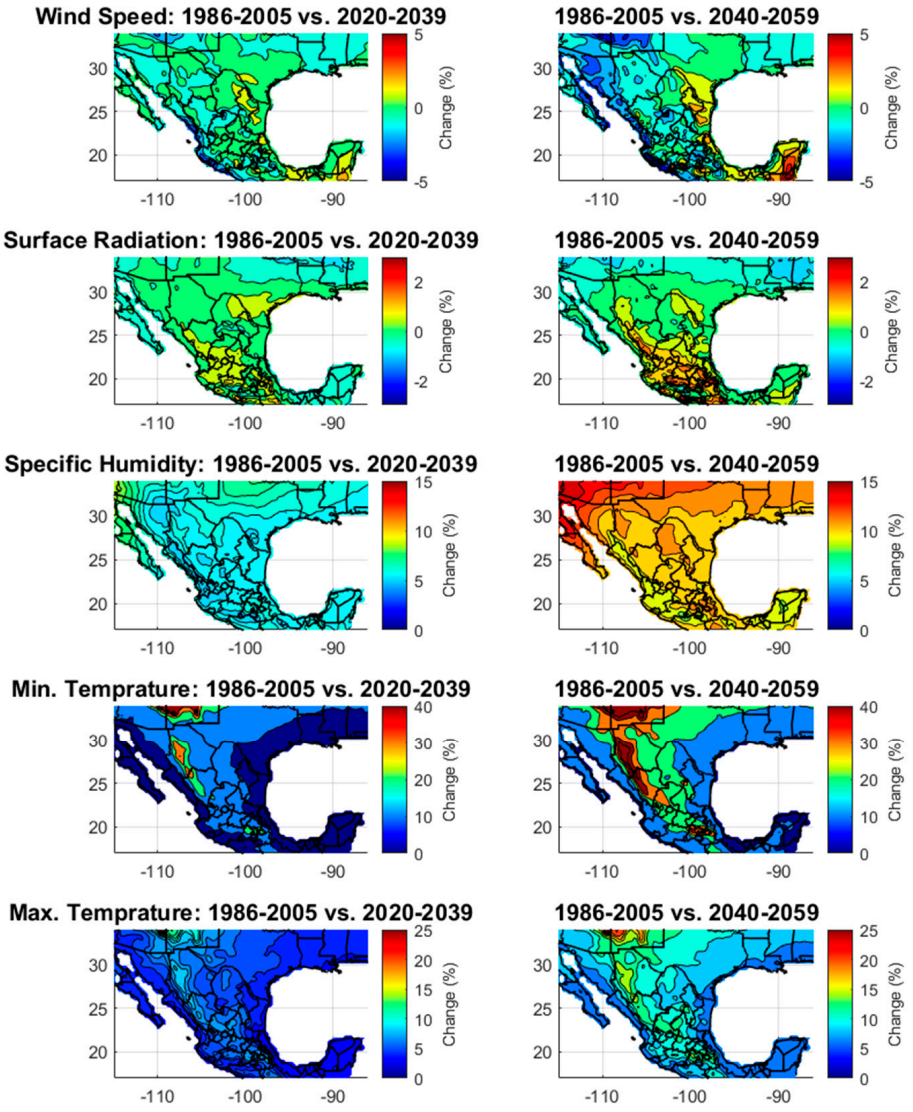

Figure 9. Annual projected changes in the six-model average for the terrestrial variables used as inputs for the PET equation for 2020–2039 (**left**) and 2040–2060 (**right**).

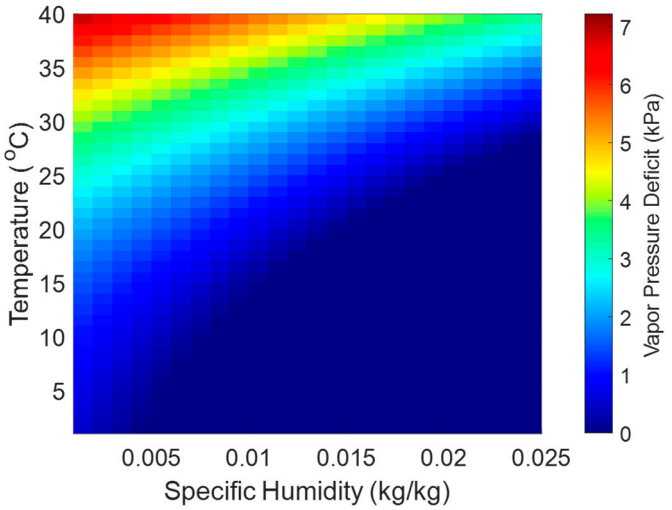

Figure 10. Sensitivity of vapor pressure deficit (VPD) to changes in temperature and specific humidity.

3.3. Monthly PET Projections

The regional inter-annual average of monthly PET, as calculated using the TerraClimate variables, is shown in Figure 11. In Figures 12 and 13, the average projected percent changes in monthly PET are shown for 2020–2039 and 2040–2059, respectively. Table 2 provides the estimated regional average monthly PET and the regional projected changes for the two projection periods. It is interesting to note that PET is projected to increase for all months except for a projected PET decrease in November–December for the 2020–2039 period. The largest projected increases are expected to occur during March–April, and the lowest increases are expected to occur in November–December. For the near future, some negative changes are projected during September–January, mainly in the northern portion of the region (Figure 12). For the far future (Figure 13), the projected negative changes in PET are seen only for November–December and in higher latitudes.

Table 2. Areal average monthly PET and projected changes for the two projection periods.

	TerraClimate 1986–2005 (mm/month)	**Projected Change 2020–2039**	**Projected Change 2040–2059**
Jan.	71	5.8%	7.9%
Feb.	91	5.7%	12.6%
Mar.	119	7.8%	13.9%
Apr.	145	9.4%	12.6%
May	161	7.9%	9.5%
Jun.	167	4.7%	7.3%
Jul.	166	3.8%	6.2%
Aug.	156	2.6%	5.2%
Sep.	129	2.3%	5.3%
Oct.	107	1.0%	6.2%
Nov.	83	−2.0%	3.8%
Dec.	68	−1.9%	5.8%
Annual	1483 (mm/year)	3.9%	8.0%

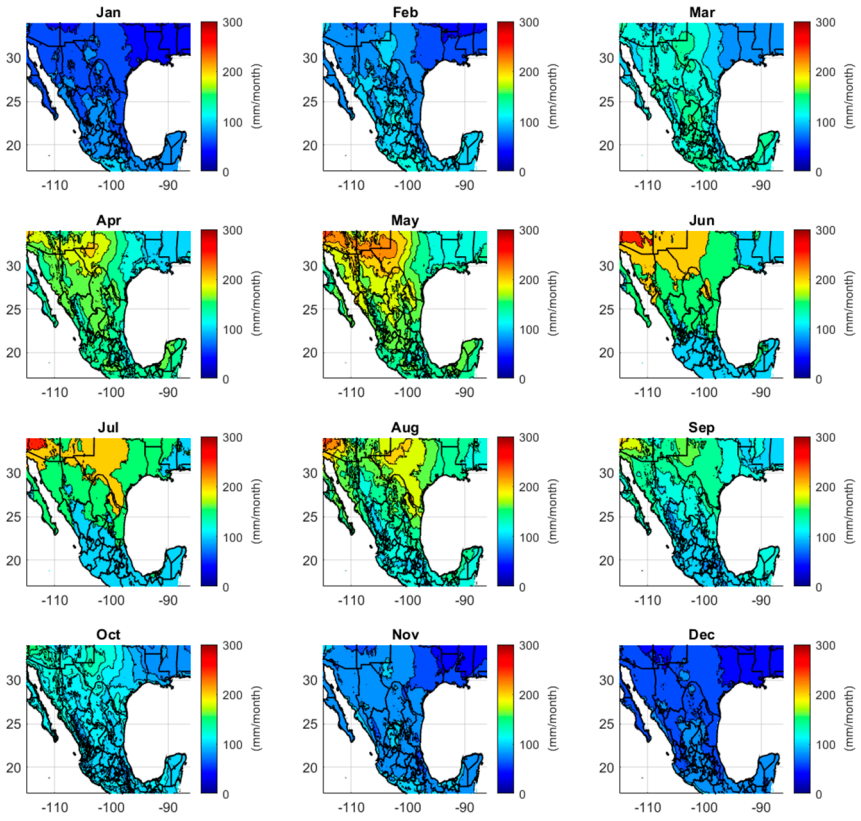

Figure 11. Historical (1986–2005) monthly average PET (mm/month) as calculated from the TerraClimate terrestrial meteorological variables.

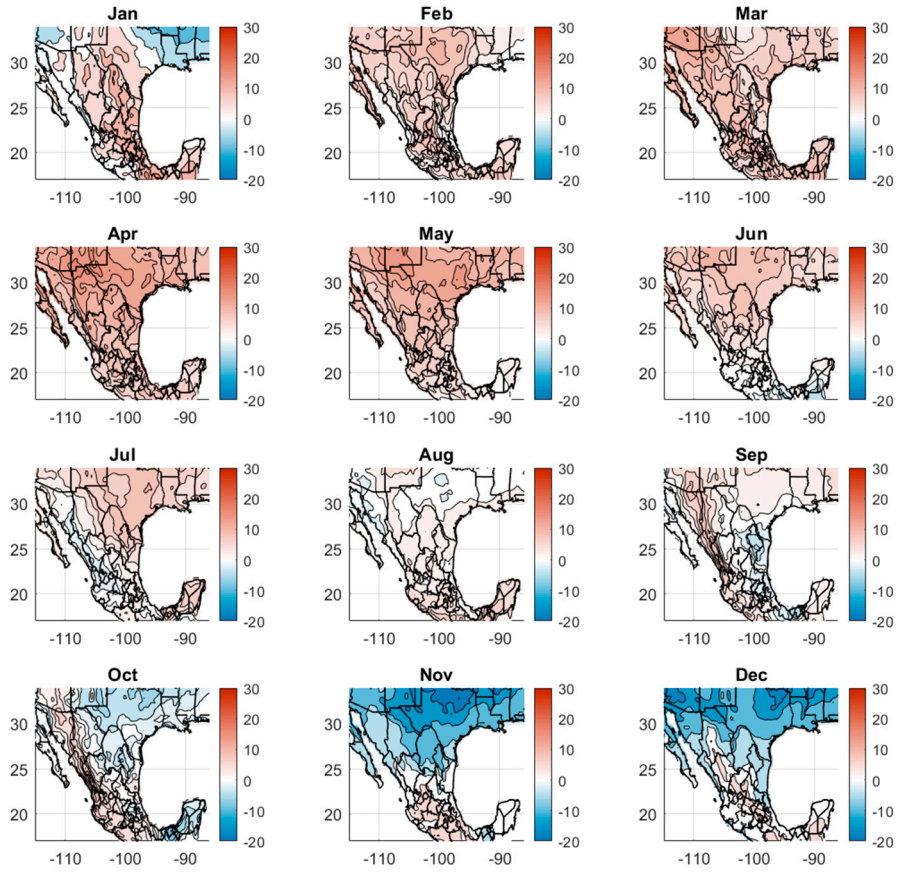

Figure 12. Average monthly changes in PET projected for 2020–2039.

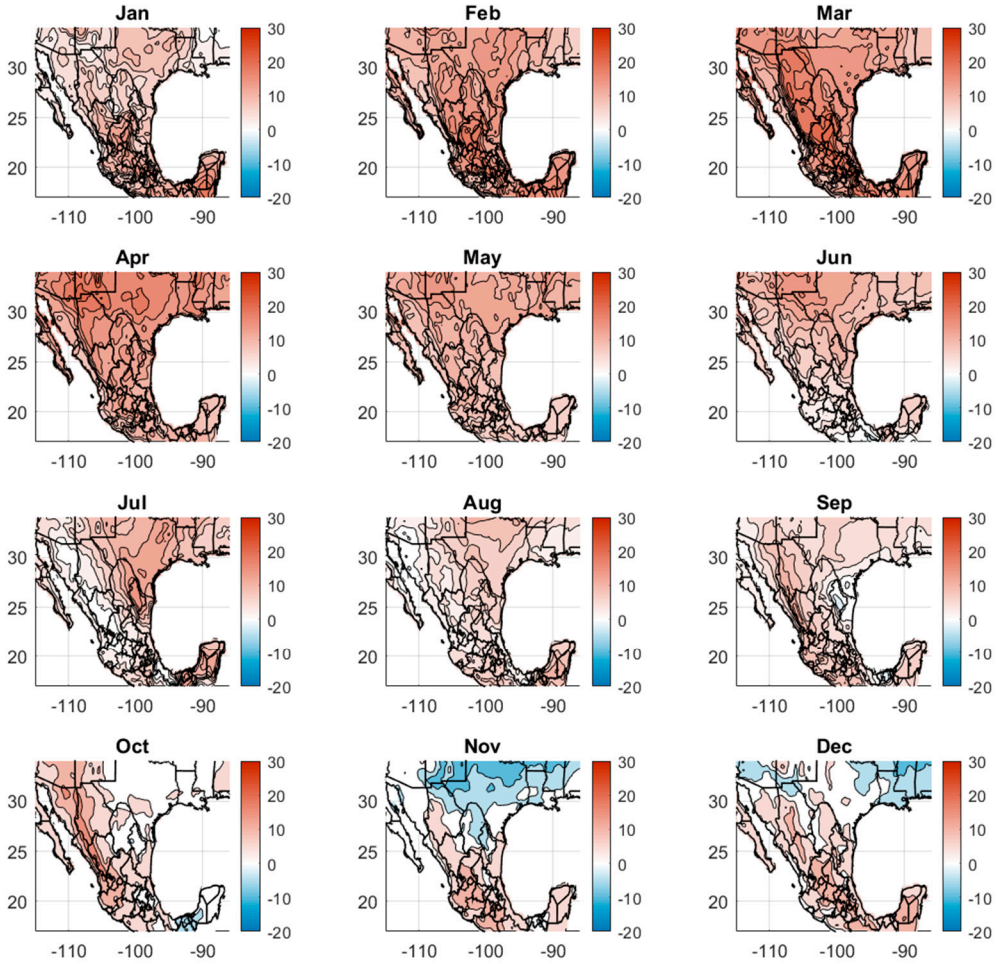

Figure 13. As in Figure 12 but projected for 2040–2059.

4. Discussion

In this study, we projected the future changes in annual and monthly PET using terrestrial meteorological variables from six dynamically downscaled climate models as inputs for the daily standardized Penman–Monteith equation. In this section, we discuss the potential caveats and sources of uncertainties in our analysis. First, we note that the study relied on six CMIP5 RCP8.5 dynamically downscaled projections from the NA-CORDEX program. Although CMIP6 GCMs have been available since 2019, at the time of writing, the NA-CORDEX simulations are the only available community-standardized dynamically downscaled regional climate model simulations for the study region. Although the analysis is limited to RCP 8.5 emission scenarios and the estimated uncertainty is based on an analysis of six ensemble members, as far as we know, these results reflect the most recently available state-of-the-art projections.

While, in some cases, the six climate projections disagree on the spatial variability of the projected changes, overall, the models are highly cross-correlated, as can be seen in Table 3. In this table, the correlation coefficient of the average areal PET historical period ranges from 0.62 to 0.97. We noted that lower correlation coefficients were obtained when the cross-correlation was derived from GCMs that were downscaled using WRF and RegCM, while when the same RCM was used, the cross-correlation coefficients were greater than 0.95.

Table 3. Correlation coefficients of the average areal PET of the historical period (1985–2005) among the six climate models.

	Had-WRF	**GFDL-WRF**	**MPI-RegCM**	**Had-RegCM**	**GFDL-RegCM**
MPI-WRF	0.96	0.95	0.68	0.70	0.62
Had-WRF		0.97	0.70	0.74	0.66
GFDL-WRF			0.69	0.74	0.70
MPI-RegCM				0.97	0.95
Had-RegCM					0.97

The PET estimates in this study are based on projected changes in terrestrial meteorological variables. These estimates do not account for the physiological adaption of vegetation to increased concentrations of atmospheric carbon dioxide. Studies have shown that various plant species have adapted to reduce stomatal conductance to decrease transpiration when atmospheric evaporative demand is high [50]. However, this adaptation is highly dependent on the vegetation type and on the ecosystems' response to elevated carbon dioxide.

With these caveats in mind, our results point to a clear increase in projected PET, and using different GCM-RCM combinations provides information about the magnitude of uncertainty in the PET projections to better inform decision making.

5. Conclusions

This study assessed the climate change impacts on PET in the Southwestern U.S. and Mexico. We used six GCM-RCM combinations of CMIP5 RCP8.5 dynamically downscaled climate projections that followed the standards set by the NA-CORDEX initiative. These climate projections were derived from three GCMs that were found to represent the study region well (HadGEM2-ES, MPI-ESM-LR, and GFDL-ESM2M), and each one was downscaled using two regional (mesoscale) models (WRF and RegCM). The terrestrial meteorological variables from these six model combinations, which include minimum and maximum temperature, wind speed, specific humidity, pressure, precipitation, and incoming short-wave radiation, were used as inputs for the FAO-56 reference crop daily PET equation. The projected future changes in the annual and monthly PET were assessed by comparing the climate models' simulations for the historical period (1986–2005) to simulations of two future projection periods (2020–2039 and 2040–2059). As a quantitative PET reference for the historical period (1986–2005), we used the 4 km-resolution monthly climatological variables available from the TerraClimate dataset.

Our study provides a range of PET projections for each grid cell of the dynamically downscaled models, representing the projected changes in the annual and monthly PET for the two projection periods. Although some of the ensemble members projected a slight decline in PET, the average 20-year annual change over the region is +4% for 2020–2039 and +7% for 2040–2059 (Table 1). The ranges of the projected average 20-year annual changes over the study area for the two projection periods were +1.4%–+8.7% and +3%–+14.2%, respectively. In general, higher values of annual changes were found for the northeast part of the region, while smaller changes were projected for areas along the Pacific coast. Despite differences in magnitude, the projected annual PET increases can be seen across the entire region and for the six climate model combinations. The main drivers for the increases are the projected warming and increase in the vapor pressure deficit.

The projected increases in PET, which represent the changes in the atmospheric evaporative demand, are substantial and likely to impact vegetation and the hydrometeorological regime in the area. Our analysis provides a probabilistic characterization of those changes, describing their inter-annual and spatial variability, in addition to the associated uncertainties. This probabilistic information can be used in local climate change risk analysis studies that assess the impacts of various agricultural practices and water resource management strategies.

Author Contributions: Conceptualization, E.S., C.L.C. and H.-I.C.; methodology, validation, and formal analysis, E.S.; data curation, L.M.F.; writing—original draft preparation, E.S.; writing—review and editing, N.P., E.T., S.M.K., H.-I.C. and C.L.C.; visualization, E.S.; project administration, H.-I.C. and C.L.C.; funding acquisition, C.L.C., H.-I.C. and E.S. All authors have read and agreed to the published version of the manuscript.

Funding: This project is funded by Fresnillo Plc. as part of a grant titled Ensemble-based Climate Assessments for Fresnillo Mining Sites in Mexico.

Data Availability Statement: Dynamically downscaled climate projections data are from https://na-cordex.org/; historical climatology data are from https://www.climatologylab.org/terraclimate.html (accessed on 18 May 2024).

Acknowledgments: Special thanks are extended to our collaborators from Fresnillo Exequiel Rolon and Alicia del Carmen Sanchez Rangel.

Conflicts of Interest: The authors declare no conflicts of interest.

References

1. Wang, B.; Biasutti, M.; Byrne, M.P.; Castro, C.; Chang, C.; Cook, K.; Fu, R.; Grimm, A.M.; Ha, K.; Hendon, H. Monsoon Climate Change Assessment. *Bull. Am. Meteorol. Soc.* **2021**, *102*, E1–E19. [CrossRef]
2. Pascale, S.; Boos, W.R.; Bordoni, S.; Delworth, T.L.; Kapnick, S.B.; Murakami, H.; Vecchi, G.A.; Zhang, W. Weakening of the North American monsoon with global warming. *Nat. Clim. Chang.* **2017**, *7*, 806–812. [CrossRef]
3. Pascale, S.; Carvalho, L.; Adams, D.; Castro, C.; Cavalcanti, I. Current and Future Variations of the Monsoons of the Americas in a Warming Climate. *Curr. Clim. Chang. Rep.* **2019**, *5*, 125–144. [CrossRef]
4. Hernandez, M.; Chen, L. Future land precipitation changes over the North American Monsoon region usingCMIP5 and CMIP6 simulations. *J. Geophys. Res. Atmos.* **2022**, *127*, e2021JD035911. [CrossRef]
5. Shamir, E.; Megdal, S.; Carrillo, C.; Castro, L.C.; Chang, H.-I.; Chief, K.; Corkhill, E.F.; Eden, S.; Georgakakos, P.K.; Nelson, M.K.; et al. Climate change and water resources management in the Upper Santa Cruz River, Arizona. *J. Hydrol.* **2015**, *521*, 18–33. [CrossRef]
6. Shamir, E.; Tapia-Villaseñor, E.M.; Cruz-Ayala, M.-B.; Megdal, S.B. A Review of Climate Change Impacts on the USA-Mexico Transboundary Santa Cruz River Basin. *Water* **2021**, *13*, 1390. [CrossRef]
7. Hu, H.; Dominguez, F. Evaluation of oceanic and terrestrial sources of moisture for the North American monsoon using numerical models and precipitation stable isotopes. *J. Hydrometeorol.* **2015**, *16*, 19–35. [CrossRef]
8. Feng, X.; Houser, P. Quantifying the strength of land–atmosphere coupling in the 2004 North American monsoon. *Atmos. Sci. Lett.* **2015**, *16*, 391–397. [CrossRef]
9. McVicar, T.R.; Roderick, M.L.; Donohue, R.J.; Li, L.T.; Van Niel, T.G.; Thomas, A.; Grieser, J.; Jhajharia, D.; Himri, Y.; Mahowald, N.M.; et al. Global review and synthesis of trends in observed terrestrial near-surface wind speeds: Implications for evaporation. *J. Hydrol.* **2012**, *416–417*, 182–205. [CrossRef]
10. Ruiz-Alvarez, O.; Singh, V.P.; Enciso-Medina, J.; Munster, C.; Kaiser, R.; Ontiveros-Capurata, R.E.; Diaz-Garcia, L.A.; Costa dos Santos, C.A. Spatio-temporal trends in monthly pan evaporation in Aguascalientes, Mexico. *Theor. Appl. Climatol.* **2019**, *136*, 775–789. [CrossRef]
11. Magallanes Quintanar, R.; López Hernández, A.M.; Galván-Tejada, C.E. Evaporation analysis and climate change in central México. *Nova Sci.* **2017**, *9*, 76–93. [CrossRef]
12. Breña-Naranjo, J.; Laverde-Barajas, M.; Pedrozo-Acuña, A. Changes in pan evaporation in Mexico from 1961 to 2010. *Int. J. Climatol.* **2016**, *37*, 204–213. [CrossRef]
13. Blanco-Macías, F.; Valdez-Cepeda, R.D.; Magallanes-Quintanar, R. Pan evaporation analysis in central Mexico: Trends, self-affinity and important frequencies. *Int. J. Phys. Sci.* **2011**, *6*, 540–549.
14. Groisman, P.Y.; Knight, R.W.; Karl, T.R.; Easterling, D.R.; Sun, B.; Lawrimore, J.H. Contemporary Changes of the Hydrological Cycle over the Contiguous United States: Trends Derived from In Situ Observations. *J. Hydrometeorol.* **2004**, *5*, 64–85. [CrossRef]
15. Cuervo-Robayo, A.P.; Ureta, C.; Gómez-Albores, M.A.; Meneses-Mosquera, A.K.; Tellez-Valdes, O.; Martinez-Meyer, E. One hundred years of climate change in Mexico. *PLoS ONE* **2020**, *15*, e0209808. [CrossRef] [PubMed]
16. Roderick, M.L.; Hobbins, M.T.; Farquhar, G.D. Pan evaporation trends and the terrestrial water balance II. Energy balance and interpretation. *Geogr. Compass* **2009**, *3*, 761–780. [CrossRef]
17. Stanhill, G.; Cohen, S. Global dimming: A review of the evidence for a widespread and significant reduction in global radiation with discussion of its probable causes and possible agricultural consequences. *Agric. For. Meteorol.* **2001**, *107*, 255–278. [CrossRef]
18. Pryor, S.C.; Barthelmie, R.J.; Young, D.T.; Takle, E.S.; Arritt, R.W.; Flory, D.; Gutowski, W.J.; Nunes, A.; Roads, J. Wind speed trends over the contiguous United States. *J. Geophys. Res.* **2009**, *114*, D14105. [CrossRef]
19. Hobbins, M.T.; Ramírez, J.A.; Brown, T.C. Trends in pan evaporation and actual evapotranspiration across the conterminous US: Paradoxical or complementary? *Geophys. Res. Lett.* **2004**, *31*, 405–407. [CrossRef]
20. Brutsaert, W.; Parlange, M. Hydrologic cycle explains the evaporation paradox. *Nature* **1998**, *396*, 30. [CrossRef]

21. Cook, B.I.; Smerdon, J.E.; Seager, R.; Coats, S. Global warming and 21st century drying. *Clim. Dyn.* **2014**, *43*, 2607–2627. [CrossRef]
22. Dewes, C.F.; Rangwala, I.; Barsugli, J.J.; Hobbins, M.T.; Kumar, S. Drought risk assessment under climate change is sensitive to methodological choices for the estimation of evaporative demand. *PLoS ONE* **2017**, *12*, e0174045. [CrossRef]
23. Ficklin, D.L.; Abatzoglou, J.T.; Robeson, S.M.; Dufficy, A. The influence of climate model biases on projections of aridity and drought. *J. Clim.* **2016**, *29*, 1269–1285. [CrossRef]
24. Martínez-Sifuentes, A.R.; Trucíos-Caciano, R.; Rodríguez-Moreno, V.M.; Villanueva-Díaz, J.; Estrada-Ávalos, J. The Impact of Climate Change on Evapotranspiration and Flow in a Major Basin in Northern Mexico. *Sustainability* **2023**, *15*, 847. [CrossRef]
25. Mundo-Molina, M. Climate change effects on Evapotranspiration in Mexico. *Am. J. Clim. Chang.* **2015**, *4*, 163–172. [CrossRef]
26. Castro, L.C.; Chang, H.-I.; Dominguez, F.; Carrillo, C.; Schemm, J.-K.; Juang, H.-M.H. Can a regional climate model improve the ability to forecast the North American Monsoon? *J. Clim.* **2012**, *25*, 8212–8236. [CrossRef]
27. Castro, L.C. Assessing climate change impacts for DoD Installations in the Southwest United States during the warm season. In *A Final Report to Strategic Environmental Research and Development Program (SERDP) Project Number RC-2205*; Office of the Deputy Assistant Secretary of Defense: Washington, DC, USA, 2017; 128p.
28. Bukovsky, M.S.; Gochis, D.J.; Mearns, L.O. Towards assessing NARCCAP regional climate model credibility for the North American monsoon: Current climate simulations. *J. Clim.* **2013**, *26*, 8802–8826. [CrossRef]
29. Bukovsky, M.S.; Carrillo, C.M.; Gochis, D.J.; Hammerling, D.M.; McCrary, R.R.; Mearns, L.O. Toward Assessing NARCCAP Regional Climate Model Credibility for the North American Monsoon: Future Climate Simulations. *J. Clim.* **2015**, *28*, 6707–6728. [CrossRef]
30. Geil, K.L.; Serra, Y.L.; Zeng, X. Assessment of CMIP5 model simulations of the North American Monsoon system. *J. Clim.* **2013**, *26*, 8787–8801. [CrossRef]
31. Prein, A.F.; Langhans, W.; Fosser, G.; Ferrone, A.; Ban, N.; Goergen, K.; Keller, M.; Tölle, M.; Gutjahr, O.; Feser, F.; et al. A review on regional convection-permitting climate modeling: Demonstrations, prospects, and challenges. *Rev. Geophys.* **2015**, *53*, 323–361. [CrossRef]
32. Qing, Y.; Wang, S. Multi-decadal convection-permitting climate projections for China's Greater Bay Area and surroundings. *Clim. Dyn.* **2021**, *57*, 415–434. [CrossRef]
33. Chang, H.-I.; Castro, C.L.; Carrillo, C.; Dominguez, F. The more extreme nature of U.S. warm season climate in the recent observational record and two "well performing" dynamically downscaled CMIP3 models. *J. Geophys. Res.* **2015**, *120*, 8244–8263. [CrossRef]
34. Kendon, E.J.; Ban, N.; Roberts, N.M.; Fowler, H.J.; Roberts, M.J.; Chan, S.C.; Evans, J.P.; Fosser, G.; Wilkinson, J.M. Do convection-permitting regional climate models improve projections of future precipitation change? *Bull. Am. Meteorol. Soc.* **2017**, *98*, 79–93. [CrossRef]
35. Abatzoglou, J.T.; Dobrowski, S.Z.; Parks, S.A.; Hegewisch, K.C. Terraclimate, a high-resolution global dataset of monthly climate and climatic water balance from 1958–2015. *Sci. Data* **2018**, *5*, 170191. [CrossRef] [PubMed]
36. Mearns, L.O.; McGinnis, S.; Korytina, D.; Arritt, R.; Biner, S.; Bukovsky, M.; Chang, H.-I.; Christensen, O.; Herzmann, D.; Jiao, Y.; et al. *The NA-CORDEX Dataset, Version 1.0*; NCAR Climate Data Gateway: Boulder, CO, USA, 2017. [CrossRef]
37. Bukovsky, M.S.; Mearns, L.O. Regional climate change projections from NA-CORDEX and their relation to climate sensitivity. *Clim. Chang.* **2020**, *162*, 645–665. [CrossRef]
38. Sheffield, J.; Barrett, A.P.; Colle, B.; Fernando, D.N.; Fu, R.; Geil, K.L.; Hu, Q.; Kinter, J.; Kumar, S.; Langenbrunner, B.; et al. North American Climate in CMIP5 Experiments. Part I: Evaluation of Historical Simulations of Continental and Regional Climatology. *J. Clim.* **2013**, *26*, 9209–9245. [CrossRef]
39. Sheffield, J.; Camargo, S.J.; Fu, R.; Hu, Q.; Jiang, X.; Johnson, N.; Karnauskas, K.B.; Kim, S.T.; Kinter, J.; Kumar, S.; et al. North American Climate in CMIP5 Experiments. Part II: Evaluation of Historical Simulations of Intraseasonal to Decadal Variability. *J. Clim.* **2013**, *26*, 9247–9290. [CrossRef]
40. Lynn, E.; Chair, C.; O'Daly, W.; Keeley, F.; Dsiwm, D.; Woled, J. *Perspectives and Guidance for Climate Change Analysis*; California Department of Water Resources (DWR) Climate Change Technical Advisory Group (CCTAG): Sacramento, CA, USA, 2015; Volume 142.
41. Gupta, N.; Bearup, L.; Jacobs, K.; Halper, E.; Castro, C.; Chang, H.-I.; Fonseca, J. Stakeholder-Informed Hydroclimate Scenario Modeling in the Lower Santa Cruz River Basin for Water Resource Management. *Water* **2023**, *15*, 1884. [CrossRef]
42. Bearup, L.; Gangopadhyay, S.; Mikkelson, K. *Lower Santa Cruz River Basin Study Hydroclimate Analysis*; A Technical Memorandum No. ENV-2021-35; Bureau of Reclamation: Denver, CO, USA, 2021.
43. Tapia-Villaseñor, E.M.; Shamir, E.; Megdal, S.B.; Petersen-Perlman, J.D. Impacts of Variable Climate and Effluent Flows on the Transboundary Santa Cruz Aquifer. *J. Am. Water Resour. Assoc.* **2020**, *56*, 409–430. [CrossRef]
44. Shamir, E.; Halper, E. Estimating Climatic Change Impacts on Water Resources in Arid Environments: The Role of Downscaling Methodology, Research and Development Office, Science and Technology Program, Final Report ST-2019-9039-01. 2019. Available online: https://www.hrcwater.org/wp-content/uploads/2019/05/Science-and-Tech-Proj-9039-Final-Report.pdf (accessed on 18 May 2024).
45. Shamir, E.; Halper, E.; Modrick, T.; Georgakakos, K.P.; Chang, H.-I.; Lahmers, T.M.; Castro, C. Statistical and dynamical downscaling impact on projected hydrologic assessment in arid environment: A case study from Bill Williams River basin and

Alamo Lake Arizona. *J. Hydrol.* **2019**, *X2*, 1000019. Available online: http://www.elsevier.com/locate/hydroa (accessed on 18 May 2024). [CrossRef]
46. Skamarock, W.C.; Klemp, J.B.; Dudhia, J.; Gill, D.O.; Barker, D.M.; Wang, W.; Powers, J.G. *A Description of the Advanced Research WRF Version 2*; NCAR Tech.Note NCAR/TN-468+STR; University Corporation for Atmospheric Research: Boulder, CO, USA, 2005.
47. Allen, R.G.; Pereira, L.S.; Raes, D.; Smith, M. *Crop Evapotranspiration Guidelines for Computing Crop Water Requirements, FAO Irrigation and Drainage Paper 56*; Food and Agriculture Organization of the United Nations: Roma, Italy, 1998.
48. Shi, L.; Feng, P.; Wang, B.; Liu, D.L.; Cleverly, J.; Fang, Q.; Yu, Q. Projecting potential evapotranspiration change and quantifying its uncertainty under future climate scenarios: A case study in southeastern Australia. *J. Hydrol.* **2020**, *584*, 124756. [CrossRef]
49. Donohue, R.J.; McVicar, T.R.; Roderick, M.L. Assessing the ability of potential evaporation formulations to capture the dynamics in evaporative demand within a changing climate. *J. Hydrol.* **2010**, *386*, 186–197. [CrossRef]
50. Vicente-Serrano, S.M.; Miralles, D.G.; McDowell, N.; Brodribb, T.; Domínguez-Castro, F.; Leung, R.; Koppa, A. The uncertain role of rising atmospheric CO_2 on global plant transpiration. *Earth-Sci. Rev.* **2022**, *230*, 104055. [CrossRef]

Disclaimer/Publisher's Note: The statements, opinions and data contained in all publications are solely those of the individual author(s) and contributor(s) and not of MDPI and/or the editor(s). MDPI and/or the editor(s) disclaim responsibility for any injury to people or property resulting from any ideas, methods, instructions or products referred to in the content.